



Probing the Properties of the Pulsar Wind in the Gamma-Ray Binary HESS J0632+057 with *NuSTAR* and VERITAS Observations

A. Archer¹, W. Benbow² , R. Bird³ , A. Brill⁴, R. Brose^{5,16}, M. Buchovecky³, J. L. Christiansen⁶, A. J. Chromey⁷, W. Cui^{8,9}, A. Falcone¹⁰, Q. Feng⁴ , J. P. Finley¹¹, L. Fortson¹² , A. Furniss¹³ , A. Gent¹⁴, G. H. Gillanders¹⁵ , C. Giuri¹⁶, O. Gueta¹⁶, D. Hanna¹⁷ , T. Hassan¹⁶, O. Hervet¹⁸, J. Holder¹⁹, G. Hughes², T. B. Humensky⁴, P. Kaaret²⁰ , N. Kelley-Hoskins¹⁶, M. Kertzman¹, D. Kieda²¹ , M. Krause¹⁶ , M. J. Lang¹⁵, G. Maier¹⁶ , P. Moriarty¹⁵, R. Mukherjee²², D. Nieto²³ , M. Nievas-Rosillo¹⁶, S. O'Brien¹⁷, R. A. Ong³, A. N. Otte¹⁴, N. Park²⁴ , A. Petrashyk⁴, K. Pfrang¹⁶, M. Pohl^{5,16} , R. R. Prado¹⁶ , E. Pueschel¹⁶ , J. Quinn²⁵, K. Ragan¹⁷, P. T. Reynolds²⁶, D. Ribeiro⁴, G. T. Richards¹⁹, E. Roache², I. Sadeh¹⁶, M. Santander²⁷ , S. Schlenstedt²⁸, G. H. Sembroski¹¹, I. Sushch⁵ , A. Weinstein⁷, P. Wilcox²⁰ , A. Wilhelm^{5,16}, D. A. Williams¹⁸, T. J. Williamson¹⁹

(VERITAS Collaboration),

and

C. J. Hailey²⁹, S. Mandel²⁹, and K. Mori²⁹

(NuSTAR Collaboration)

¹ Department of Physics and Astronomy, DePauw University, Greencastle, IN 46135-0037, USA

² Center for Astrophysics|Harvard & Smithsonian, Cambridge, MA 02138, USA

³ Department of Physics and Astronomy, University of California, Los Angeles, CA 90095, USA

⁴ Physics Department, Columbia University, New York, NY 10027, USA

⁵ Institute of Physics and Astronomy, University of Potsdam, D-14476 Potsdam-Golm, Germany

⁶ Physics Department, California Polytechnic State University, San Luis Obispo, CA 94307, USA

⁷ Department of Physics and Astronomy, Iowa State University, Ames, IA 50011, USA

⁸ Department of Physics and Astronomy, Purdue University, West Lafayette, IN 47907, USA

⁹ Department of Physics and Center for Astrophysics, Tsinghua University, Beijing 100084, People's Republic of China

¹⁰ Department of Astronomy and Astrophysics, 525 Davey Lab, Pennsylvania State University, University Park, PA 16802, USA

¹¹ Department of Physics and Astronomy, Purdue University, West Lafayette, IN 47907, USA

¹² School of Physics and Astronomy, University of Minnesota, Minneapolis, MN 55455, USA

¹³ Department of Physics, California State University—East Bay, Hayward, CA 94542, USA

¹⁴ School of Physics and Center for Relativistic Astrophysics, Georgia Institute of Technology, 837 State Street NW, Atlanta, GA 30332-0430, USA

¹⁵ School of Physics, National University of Ireland Galway, University Road, Galway, Ireland

¹⁶ DESY, Platanenallee 6, D-15738 Zeuthen, Germany; raul.prado@desy.de

¹⁷ Physics Department, McGill University, Montreal, QC H3A 2T8, Canada

¹⁸ Santa Cruz Institute for Particle Physics and Department of Physics, University of California, Santa Cruz, CA 95064, USA

¹⁹ Department of Physics and Astronomy and the Bartol Research Institute, University of Delaware, Newark, DE 19716, USA

²⁰ Department of Physics and Astronomy, University of Iowa, Van Allen Hall, Iowa City, IA 52242, USA

²¹ Department of Physics and Astronomy, University of Utah, Salt Lake City, UT 84112, USA

²² Department of Physics and Astronomy, Barnard College, Columbia University, NY 10027, USA

²³ Institute of Particle and Cosmos Physics, Universidad Complutense de Madrid, E-28040 Madrid, Spain

²⁴ WIPAC and Department of Physics, University of Wisconsin-Madison, Madison WI, USA

²⁵ School of Physics, University College Dublin, Belfield, Dublin 4, Ireland

²⁶ Department of Physical Sciences, Cork Institute of Technology, Bishopstown, Cork, Ireland

²⁷ Department of Physics and Astronomy, University of Alabama, Tuscaloosa, AL 35487, USA

²⁸ CTAO, Saupfercheckweg 1, D-69117 Heidelberg, Germany

²⁹ Columbia Astrophysics Laboratory, Columbia University, New York, NY, USA

Received 2019 July 16; revised 2019 October 28; accepted 2019 November 19; published 2020 January 15

Abstract

HESS J0632+057 is a gamma-ray binary composed of a compact object orbiting a Be star with a period of about 315 days. Extensive X-ray and TeV gamma-ray observations have revealed a peculiar light curve containing two peaks, separated by a dip. We present the results of simultaneous observations in hard X-rays with *NuSTAR* and in TeV gamma-rays with VERITAS, performed in 2017 November and December. These observations correspond to the orbital phases $\phi \approx 0.22$ and 0.3, where the fluxes are rising toward the first light-curve peak. A significant variation of the spectral index from 1.77 ± 0.05 to 1.56 ± 0.05 is observed in the X-ray data. The multiwavelength spectral energy distributions (SED) derived from the observations are interpreted in terms of a leptonic model, in which the compact object is assumed to be a pulsar and nonthermal radiation is emitted by high-energy electrons accelerated at the shock formed by the collision between the stellar and pulsar wind. The results of the SED fitting show that our data can be consistently described within this scenario, and allow us to estimate the magnetization of the pulsar wind at the location of the shock formation. The constraints on the pulsar wind magnetization provided by our results are shown to be consistent with those obtained from other systems.

Unified Astronomy Thesaurus concepts: [Gamma-ray sources \(633\)](#); [High mass X-ray binary stars \(733\)](#); [Gamma-ray astronomy \(628\)](#); [Particle astrophysics \(96\)](#); [Pulsars \(1306\)](#)

1. Introduction

Gamma-ray binaries are systems composed of a massive star and a compact object in which the nonthermal luminosity is dominated by the gamma-ray emission (>1 MeV) (Dubus 2013). Objects of this class are extremely rare, and currently only a handful of sources have been unambiguously identified as gamma-ray binaries: PSR B1259-63, LS 5039, LS I+61 303, HESS J0632+057, 1FGL J1018.6–5856, LMC P3, PSR J2032+4127 (Paredes & Bordas 2019), and 3FGL J1405.4-6119 (Corbet et al. 2019). All of these systems host compact objects, either neutron stars or black holes, orbiting a massive star of O or B type. Their orbital periods vary substantially, spanning from 3.9 days (LS 5039) to ~ 50 yr (PSR J2032+4127). Only PSR B1259-63 and PSR J2032+4127 contain known radio pulsars, while the nature of the compact object in the remaining systems is still unknown.

Two distinct scenarios are commonly invoked to explain the origin of the nonthermal emission in gamma-ray binaries. In objects known as *microquasars*, the accretion of stellar material onto the compact object produces relativistic jets where particles are accelerated to high energies and can radiate in the gamma-ray band (Mirabel & Rodríguez 1998). Where the system hosts a pulsar, the spin-down power of a young pulsar is transferred to high-energy particles through the acceleration of electron pairs from the pulsar wind in the termination shock formed by the interaction of the pulsar and the stellar winds (Tavani & Arons 1997).

HESS J0632+057 was first detected as an unidentified point-like source during H.E.S.S. observations of the Monoceros region (Aharonian et al. 2007). Its binary nature in association with the Be star MWC 148 was suggested at first and supported later by *XMM-Newton* observations in X-rays (Hinton et al. 2009). Subsequent observations by VERITAS did not lead to a detection (Acciari et al. 2009), indicating a substantial flux variability, which is characteristic of gamma-ray binaries. Since then, extensive observations have been performed in soft X-rays (Falcone et al. 2010) and the TeV gamma-ray band (Aleksić et al. 2012; Aliu et al. 2014). Both X-ray and gamma-ray light curves present two clear periodic peaks around $\phi \approx 0.3$ – 0.4 and $\phi \approx 0.6$ – 0.8 when folded to an orbital period of around 315–320 days (Aliu et al. 2014). The system is uncommonly faint in the GeV band compared with other gamma-ray binaries, having been detected only recently in *Fermi*-LAT data (Li et al. 2017).

Aragona et al. (2010) estimated the distance of the system to be 1.1–1.7 kpc through optical spectroscopy of the companion star MWC 148. The orbital period of $P_{\text{orb}} = 321$ days was first derived by Bongiorno et al. (2011) using X-ray light-curve data, and was later refined to be $P_{\text{orb}} = 315^{+6}_{-4}$ by Aliu et al. (2014). Two distinct orbital solutions have been proposed by Casares et al. (2012) and, more recently, by Moritani et al. (2018). Both studies follow similar methodologies based on optical spectroscopic data; however, Moritani et al. (2018) uses a more extensive data set, which results in a set of orbital parameters entirely different from those by Casares et al. (2012).

The nature of the compact object in HESS J0632+057 is still uncertain, as the implications of the two orbital solutions point in the opposite directions. Moritani et al. (2018) suggest that the mass of the compact object must be consistent with the pulsar scenario ($M_{\text{co}} < 2.5 M_{\odot}$) unless the inclination of the

system is extremely small ($<3^{\circ}$). On the other hand, the solution by Casares et al. (2012) favors the black hole scenario with $M_{\text{co}} > 2.1 M_{\odot}$ (Zamanov et al. 2017), being only marginally compatible with the pulsar scenario. In addition to the mass functions, indirect evidence of the pulsar scenario can only be claimed by comparing the observational features of HESS J0632+057 to other known sources, especially PSR B1259-63, in which the compact object is a known pulsar.

In this paper, we present simultaneous observations in X-ray by *NuSTAR* and TeV gamma-ray by VERITAS during 2017 November and December. These observations correspond to $\phi \approx 0.22$ and 0.30 , respectively, when the X-ray and TeV fluxes are rising toward the first flux peak (Aliu et al. 2014). The pulsar scenario is probed by fitting the spectral energy distribution (SED) to a model in which the nonthermal emission is assumed to be produced by electrons from the pulsar wind that are accelerated at the termination shock formed by the collision of the stellar and pulsar wind. The X-ray and TeV gamma-ray spectra are assumed to be produced through synchrotron radiation and inverse Compton scattering (ICS) of stellar photons, respectively. Because the distance between the Be star and the compact object at the time of the observations is substantially larger than the estimated size of the circumstellar disk, the model relies on a few assumptions about the properties of the polar stellar wind, neglecting the disk component. As the result of the model fitting, we obtain a relation between the pulsar spin-down luminosity (L_{sd}) and the pulsar-wind magnetization (σ) that is consistent with theoretical expectations. This result shows that our data can be satisfactorily described within the pulsar hypothesis.

The observations and data analysis are first described in Sections 2 and 3. In Section 4 we describe the system parameters, including both orbital solutions, and define the sets of parameters adopted in this work. The model based on the pulsar-wind scenario is described in Section 5, and the results of the SED model fitting in Section 6. Finally, we summarize and discuss the results in Section 7.

2. Observations

2.1. NuSTAR

NuSTAR is composed of a pair of co-aligned high-energy X-ray focusing telescopes with focal plane modules FPMA and FPMB, which provide an imaging resolution of $18''$ FWHM over an energy band of 3–79 keV and a characteristic 400 eV FWHM spectral resolution at 10 keV (Harrison et al. 2013). The absolute and relative timing accuracy of *NuSTAR*, after correcting for on-board clock drift, are 3 ms and $10 \mu\text{s}$, respectively (Madsen et al. 2015). *NuSTAR*'s broadband capabilities allow it to measure spectral properties such as photon indices with relatively high precision, with little to no dependency with interstellar medium absorption (N_{H}).

HESS J0632+057 was first observed by *NuSTAR* on 2017 November 22, with a 49.7 ks exposure, followed by a second observation on 2017 December 14, with a 49.6 ks exposure. Data processing and analysis was completed using the HEASOFT (V6.22) software package, including NUSTAR-DAS 06Jul17_v1.8.0; *NuSTAR* Calibration Database (CALDB) files dated 2017 August 17 were utilized.

2.2. VERITAS

VERITAS is an array of four 12 m diameter telescopes at the Fred Lawrence Whipple Observatory (Weekes et al. 2002), designed to observe gamma-ray sources in the energy range between 85 GeV and 30 TeV. The observations are performed through the detection of the Cerenkov light induced by the cascade of particles produced after the interaction of the gamma-ray photon with the atmosphere. Each telescope contains a 499 pixel photomultiplier tube camera at the focal plane, adding up to a field of view of $3^{\circ}.5$ (Holder et al. 2006). The current sensitivity of VERITAS enables detection of a source with 1% of the Crab Nebula flux within 25 hr. The angular resolution is $<0^{\circ}.1$ at 1 TeV (Park 2015).

HESS J0632+057 was observed by VERITAS for 7.4 hr between 2017 November 16 and 26, and for 6.0 hr between 2017 December 14 and 16. Observations were conducted in “wobble” mode in which the source was located at a $0^{\circ}.5$ offset from the center of the telescope’s field of view to allow simultaneous and symmetric evaluation of the background. The average elevation was $\approx 60^{\circ}$ for both periods, resulting in an energy threshold of 200 GeV.

3. Data Analysis

3.1. NuSTAR Spectral Analysis

Source photons were extracted from a $r = 30''$ circle centered on the source position at R.A. = $98^{\circ}.2472$ and decl. = $5^{\circ}.8015$ (J2000), yielding a total of 2534/2468 net counts (FPMA and FPMB combined) for the 2017 November/December observations, respectively, for a net count rate of ~ 0.02 cts s^{-1} for each detector module. Background spectra were extracted from a rectangular source-free region on the same detector chip as the source. We used `nuproducts` to generate the response matrix and ancillary response files.

NuSTAR spectra were grouped to a minimum significance of 5σ in each bin and fitted with the XSPEC (v12.9.1) package (Arnaud 1996) using χ^2 statistics. We fit NuSTAR module A and B spectra jointly in the 3–30 keV energy band, above which the background dominates. Given the previously measured column density values ($N_H \sim (2.1\text{--}4.7) \times 10^{21}$ cm^{-2}) (Moritani et al. 2018), we find that the ISM absorption is negligible above 3 keV. Therefore, NuSTAR 3–30 keV spectra allow us to determine the intrinsic continuum spectral index independently, without degeneracy with N_H .

We fit a single power-law model to the spectra. For the November observation, the best-fit photon index was $\Gamma = 1.77 \pm 0.05$ ($\chi/\text{dof} = 0.92$ for 105 dof); the 3–30 keV flux for the unabsorbed power law is $(2.42 \pm 0.13) \times 10^{-12}$ $\text{erg cm}^{-2} \text{s}^{-1}$, and the corresponding luminosity is $(5.67 \pm 0.30) \times 10^{32}$ erg s^{-1} . The December spectrum is significantly harder, with photon index $\Gamma = 1.56 \pm 0.05$ ($\chi/\text{dof} = 0.71$ for 102 dof), while 3–30 keV flux is $(2.45 \pm 0.13) \times 10^{-12}$ $\text{erg cm}^{-2} \text{s}^{-1}$, for a luminosity of $(5.75 \pm 0.30) \times 10^{32}$ erg s^{-1} . All uncertainties were calculated at 1σ intervals. Luminosity values assume a distance of 1.4 kpc.

We find no significant spectral break or cutoff in the NuSTAR spectra. The NuSTAR SED derived from the spectral analysis is shown in Figure 1 (upper panels).

3.2. NuSTAR Timing Analysis

After applying the barycentric correction to photon event files using the NuSTAR clock file, we extracted light curves from the same $r = 30''$ circular region around the source. A Bayesian block analysis yielded no time variability in the light curves during the NuSTAR observations.

To produce a power density spectrum, we used HENDRICS, one of the modules in the Stingray software package (Huppenkothen et al. 2016). HENDRICS has been specifically developed for NuSTAR timing analysis to take into account the dead time effects and observation gaps (Bachetti et al. 2015). Given that NuSTAR count rates are ~ 0.02 cts s^{-1} , the dead time effect is negligible. We binned the source light curves with a constant bin size $\Delta T = 2^{-6}$ s (0.016 s) and generated power density spectra in the 3–30 keV band. We find that the resulting power density spectra are flat with no sign of red noise or pulsation signals during either NuSTAR observation. This is consistent with other gamma-ray binaries where the X-ray emission likely originates from an intrabinary region shocked by colliding pulsar and stellar winds (Mori et al. 2017).

3.3. VERITAS Analysis

The analyses of VERITAS observations were performed at the position of the X-ray source XMMU J063259.3+054801. The data were analyzed according to the standard procedure described by Maier & Holder (2017). The images were first calibrated, cleaned (Acciari et al. 2008), and then parameterized using the Hillas criteria (Hillas 1985; Krawczynski et al. 2006; Daniel 2008). A stereoscopic technique that combines the orientation of the images from different telescopes was used to determine the arrival direction and core location of the gamma-ray shower. The energy reconstruction was performed by a lookup table method utilizing the impact distance, image size, and zenith angle.

A set of predefined cuts optimized to provide highest sensitivity for a point-like source were applied to reject background events, which are mostly composed of air showers initiated by cosmic rays. The remaining background was then estimated through the reflected region method (Fomin et al. 1994). The source was detected with a significance of 5.2 and 4.5σ for the 2017 November and December observations, respectively.

The SED derived from the VERITAS observations covers the range of 0.2–3 TeV. In Figure 1 (lower panels), we show the SED from both observations, along with the results of a fit to a single power law. The flux in the range 0.2–3 TeV, the corresponding luminosity, and the power-law index were found to be $(3.5 \pm 0.8) \times 10^{-12}$ $\text{erg cm}^{-2} \text{s}^{-1}$, $(8.1 \pm 1.9) \times 10^{32}$ erg s^{-1} and 2.9 ± 0.5 for the November observation, and $(3.4 \pm 0.8) \times 10^{-12}$ $\text{erg cm}^{-2} \text{s}^{-1}$, $(7.9 \pm 1.9) \times 10^{32}$ erg s^{-1} and 2.0 ± 0.4 for the December observation.

4. System Parameters and Orbital Solutions

Accurate knowledge of the system’s geometry and the properties of the companion star are critical ingredients for any attempt at modeling gamma-ray binaries. In this section, we summarize the available orbital solutions and the parameters related to the companion Be star, including the properties of the

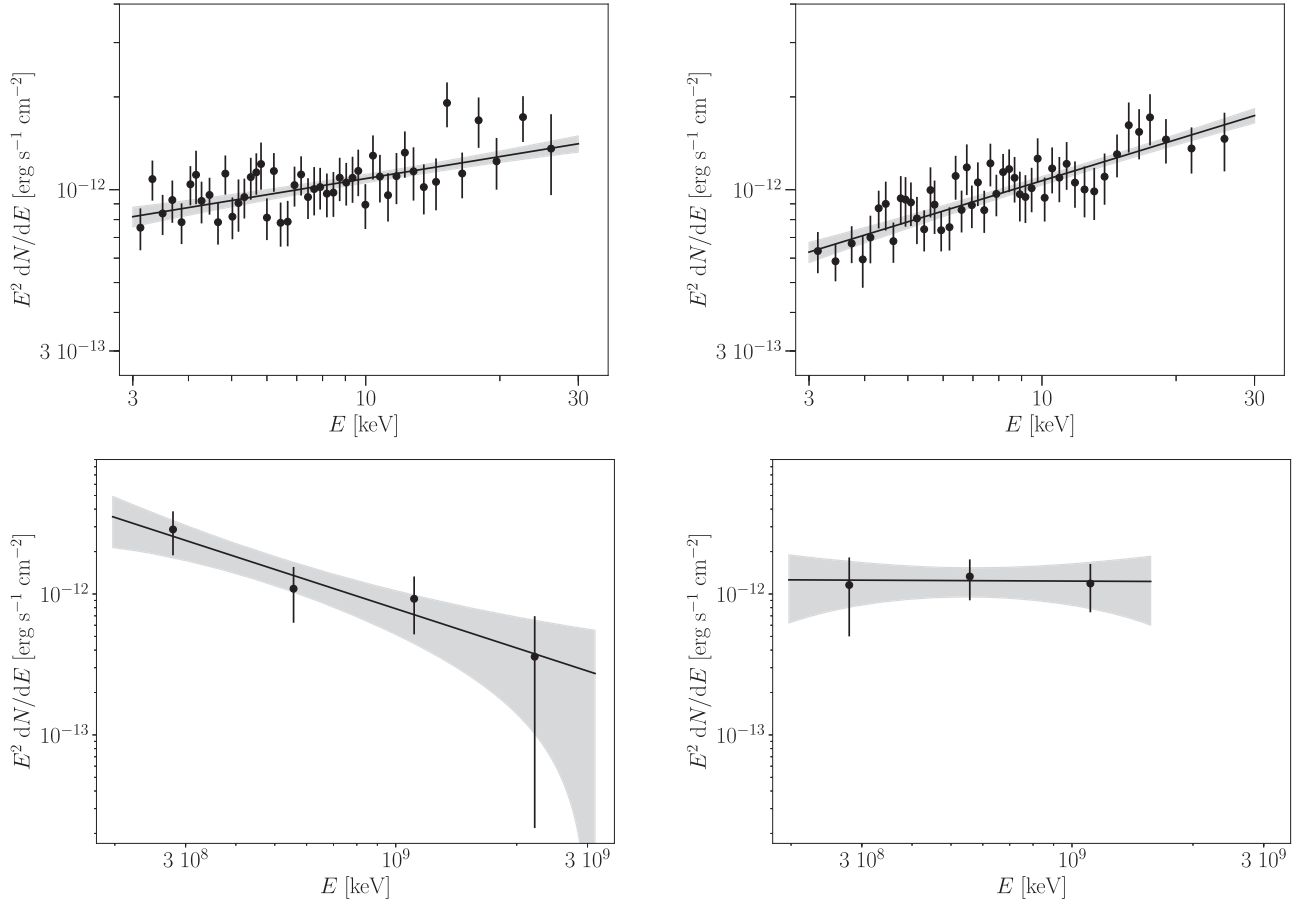


Figure 1. SED derived from *NuSTAR* (upper panels) and VERITAS (lower panels) observations from 2017 November (left) and December (right). The dashed lines show the result of the single power-law fit and the gray band its 1σ confidence interval.

stellar wind. We also describe the sets of parameters that will be assumed for the model fitting presented in the next sections.

The properties of the companion Be star MWC 148 (=HD 259440) were first derived through optical spectroscopy by Aragona et al. (2010). The effective temperature T was found to be 27.5–30.0 kK, the mass 13.2–19.0 M_{\odot} and the radius 6.0–9.6 R_{\odot} . The distance of the system was also derived to be 1.1–1.7 kpc. Based on these ranges of values, we assume $T_{\text{Be}} = 30$ kK, $R_{\text{Be}} = 7.8 R_{\odot}$ and $d = 1.4$ kpc. The mass of the star M_{Be} , however, will be allowed to vary within the derived range according to the mass function $f(M)$ obtained in the orbital solutions and the system’s inclination i .

The first orbital solution was obtained by Casares et al. (2012) through spectroscopic studies of $H\alpha$ emission lines. Recently, however, Moritani et al. (2018) proposed a distinct solution, obtained with the same methodology but with a larger data set. For the present study, both solutions will be considered and two sets of parameters will be defined. The orbital period (P_{orb}) of the system was assumed to be 321 days by Casares et al. (2012) and derived to be 313 days by Moritani et al. (2018).³⁰ Although P_{orb} is correlated to the more recent orbital parameters (Ho et al. 2017), we assume here that the impact of varying it by a few days is negligible and we will set $P_{\text{orb}} = 315$ days for both sets of parameters, following the results obtained by Aliu et al. (2014). To estimate the impact of

³⁰ From the two solutions obtained by Moritani et al. (2018), we adopted that in which the orbital period was derived from the analysis of the X-ray light curve.

Table 1
System Parameters of HESS J0632+057 as Used in This Work

	Casares et al. (2012)	Moritani et al. (2018)
e	0.83 ± 0.08	0.64 ± 0.29
ω ($^{\circ}$)	129 ± 17	271 ± 29
f (M_{\odot})	0.01	0.0024
i ($^{\circ}$)	69.5 ± 10.5	37 ± 5
a_2 (au)	$3.90^{+0.13}_{-0.22}$	$2.13^{+0.14}_{-0.17}$
P_{orb} (day)		315 ± 2
M_{psr} (M_{\odot})		1.4
M_{Be} (M_{\odot})		13.2–19.0
R_{Be} (R_{\odot})		7.8
T_{Be} (K)		30000
v_w (km s^{-1})		1500
\dot{M}_w ($M_{\odot} \text{yr}^{-1}$)		$10^{8.5 \pm 0.5}$

Note. See the text for the description and references. The MJD of $\phi = 0$ is 54857.5 as defined by Falcone et al. (2010).

the P_{orb} uncertainties on the results of our studies, we will consider an arbitrary ± 2 days uncertainty range. The sets of parameters defined for our study are shown in Table 1 and the orbit of the compact object is illustrated in Figure 2. The uncertainties shown in Table 1 were accounted for to probe the robustness of the model fitting. The uncertainties on R_{Be} and T_{Be} are not relevant and will be neglected.

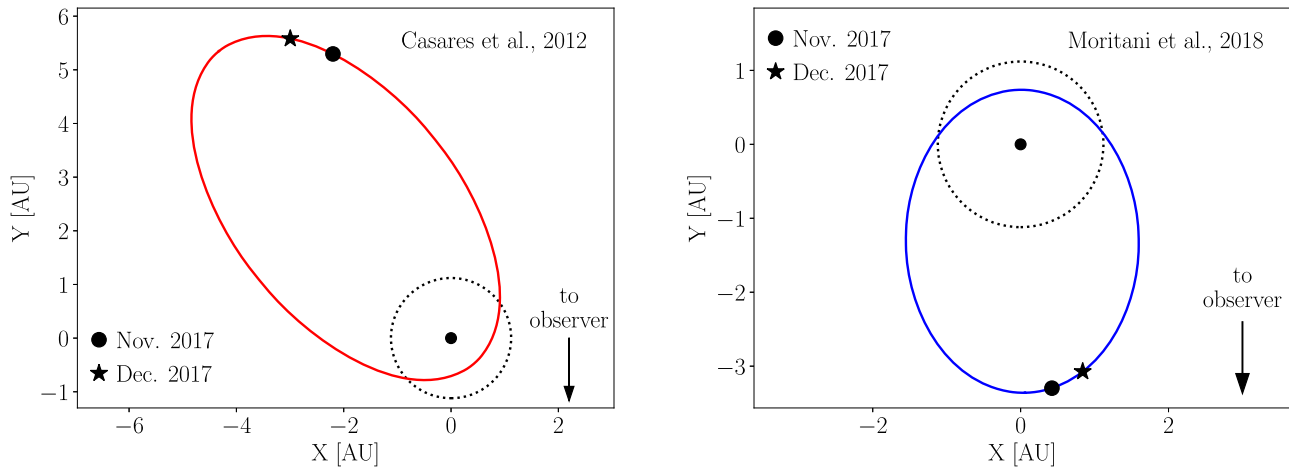


Figure 2. Illustration of the orbit of the compact object projected onto the orbital plane for Casares et al. (2012) (left) and Moritani et al. (2018) (right) solutions. The semimajor axis of the compact object (a_2) was calculated for the corresponding inclination (i) and mass function ($f(M)$) as given in Table 1. The locations of the compact object during the two sets of observations are indicated as black markers. The companion star is assumed to be in a fixed position and the estimated size of the circumstellar disk (Moritani et al. 2015; Zamanov et al. 2016) is indicated by a dashed black line.

The compact object is assumed to be a pulsar with $M_{\text{psr}} = 1.4 M_{\odot}$ in the model considered here. With this assumption, the mass function $f(M)$ from a given orbital solution constrains the relation between M_{Be} and the inclination i . Thus, the allowed range of i can be defined by imposing that M_{Be} is consistent with the range derived by Aragona et al. (2010). M_{Be} versus i is shown in Figure 3, from which we find that (a) $32^{\circ} < i < 42^{\circ}$ for the Moritani et al. (2018) solution and (b) there is no value of i allowed for the Casares et al. (2012) solution assuming the nominal value of $f(M) = 0.06$, as can be seen by the solid red line. To define a set of orbital parameters based on the Casares et al. (2012) solution, we redefine $f(M)$ to its lower bound within the quoted uncertainties, given by $f(M) = 0.06 - 0.05 = 0.01$. By doing this, we find that $i > 59^{\circ}$ becomes allowed (see the dashed red line in Figure 3). The upper bound of i will be set to 80° following the argument given by Casares et al. (2012) based on the lack of observed shell lines, which would have indicated obscuration of the star by the circumstellar disk.

In the orbital parameters defined for our study, the inclination will be taken as the center of the allowed range, with the full range being used to probe the robustness of the results. As M_{Be} is linked to the inclination through the mass function, i and M_{Be} are strongly correlated. A similar relation occurs with the semimajor axis of the pulsar orbit (a_2), as the orbital solutions directly provide $a_1 \sin i$, where $a_1/a_2 = M_{\text{psr}}/M_{\text{Be}}$. The uncertainties of a_2 indicated in Table 1 are due to the effect of varying i within its allowed range.

In shocked wind models, the properties of the stellar winds are relevant ingredients because the location of the intrabinary shock is determined by the dynamical pressure balance between the stellar and pulsar winds. For Be stars, the stellar wind is commonly described as being composed of a fast low-density polar wind and a slow dense equatorial disk wind (Waters et al. 1988). The disk properties of MWC 148 were studied by Moritani et al. (2015), Zamanov et al. (2016) through optical spectroscopy. It was found that the disk size, estimated as the radius of the $\text{H}\alpha$ emitting region, is 0.85–1.4 au. The average disk radius of 1.12 au is indicated by dotted lines in Figure 2, assuming that the disk and the orbit of the compact object are co-planar.

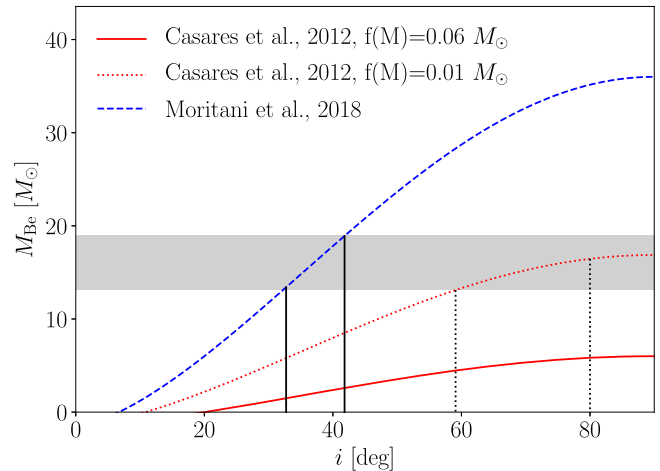


Figure 3. Mass of the companion star (M_{Be}) as a function of the inclination (i) following the mass function given by the orbital solutions. The gray band indicates the allowed range of M_{Be} derived by Aragona et al. (2010). The vertical solid and dotted lines indicate the limits of i used in this work for the Casares et al. (2012) and Moritani et al. (2018) solutions, respectively.

For the sets of observations reported here, both orbital solutions imply that the distance between the Be star and the pulsar is substantially larger than the disk size. Therefore, the influence of the disk on the shock formation in the colliding wind scenario is expected to be relevant only if the shock is located relatively close to the companion star. We will show, by the results of the model fitting, that the pulsar spin-down luminosity L_{sd} required for the latter condition is not supported by our observations. Therefore, we will neglect the interaction with the disk in our model and only the polar-wind parameters will be defined.

The velocity profile of the polar wind is approximately described by $v_w(r) = v_0 + (v_{\infty} - v_0)(1 - R_{\text{Be}}/r)$ (Waters et al. 1988), where typically $v_0 \sim 20 \text{ km s}^{-1}$ and $v_{\infty} \sim 1000\text{--}2000 \text{ km s}^{-1}$. Because $r \gg R_{\text{Be}}$ in the context of our study, we use the approximation $v_w = v_{\infty}$, assuming $v_w = 1500 \text{ km s}^{-1}$. The mass-loss rate \dot{M}_w of the wind in Be stars is only poorly constrained and it is usually assumed to be in the range $10^{-9}\text{--}10^{-8} M_{\odot} \text{ yr}^{-1}$ based on Snow (1981); Waters et al. (1988). The impact of the \dot{M}_w uncertainties on the results

of the model fitting is substantial, because the relative location of the intrabinary shock is strongly affected by this parameter. Thus, we will adopt $\dot{M}_w = 10^{-8.5} M_\odot \text{yr}^{-1}$ as a reference value and the range $10^{-9} - 10^{-8} M_\odot \text{yr}^{-1}$ will be used to provide an estimation of its uncertainties.

5. Description of the Model

Our model is based on the assumption that the compact object is a pulsar of mass $M_{\text{psr}} = 1.4 M_\odot$. The collision between the pulsar and the stellar wind creates a termination shock which is assumed to accelerate cold electron pairs from the pulsar wind to high energies. Hence, nonthermal radiation emitted by the accelerated electrons located around the apex of the shock is believed to produce the observed X-ray and gamma-ray photons through synchrotron and ICS, respectively. The pulsar spin-down luminosity, L_{sd} , is a central parameter of the model, as it drives the pulsar-wind pressure as well as the B -field strength. It is important to note that the following fitting approach is only meant to describe the observations presented in this paper with a minimum number of assumptions. The application of the same ideas to observations taken at other points in the orbit would require to take into account further processes, in particular, the effect of the circumstellar disk on the shock formation.

5.1. Shock Formation and the Pulsar-wind Magnetization

By imposing hydrodynamic balance between the pulsar and the stellar wind, the distance of the shock apex to the pulsar is given by (Harding & Gaissner 1990; Tavani & Arons 1997; Ball & Kirk 2000)

$$R_{\text{sh}} = \frac{\sqrt{\eta}}{1 + \sqrt{\eta}} D, \quad (1)$$

where

$$\eta = \frac{L_{\text{sd}}}{\dot{M} v_w c}, \quad (2)$$

and D is the distance between both objects. \dot{M} and v_w are the mass-loss rate and the wind velocity assumed for the polar component of the stellar wind. The circumstellar disk component of the wind is neglected here because the distance between the objects is much larger than the size of the disk as estimated by Moritani et al. (2015), Zamanov et al. (2016). The influence of the disk, if present, would move the shock position closer to the pulsar, changing the properties of the nonthermal emission. The same effect would be observed by assuming different values of \dot{M} , while still neglecting the disk component of the wind. Thus, in this model, the effect of disk interactions on the emission features are estimated by changing \dot{M} within its uncertainties.

The particle acceleration, and consequently, nonthermal emission, is assumed to occur in a relatively small region around the shock apex, and therefore, the shock morphology will be neglected. This assumption is supported by the results of hydrodynamical simulations of the gamma-ray binary LS 5039 (Dubus et al. 2015).

The relativistic electron pairs from the pulsar wind are accelerated at the termination shock, forming the high-energy electron population, upstream to the shock that is responsible for the nonthermal radiation. Following Kennel & Coroniti

(1984a, 1984b), the B -field upstream of the shock is given by

$$B = \sqrt{\frac{L_{\text{sd}} \sigma}{R_{\text{sh}} c (1 + \sigma)}} \left(1 + \frac{1}{u^2}\right), \quad (3)$$

where u is the radial four-velocity of the wind downstream from the shock, given by

$$u^2 = \frac{8\sigma^2 + 10\sigma + 1}{16(\sigma + 1)} + \frac{[64\sigma^2(\sigma + 1)^2 + 20\sigma(\sigma + 1) + 1]^{1/2}}{16(\sigma + 1)}. \quad (4)$$

The magnetization of the wind σ is commonly assumed to depend on the distance from the pulsar, as $\sigma \propto R_{\text{sh}}^{-\alpha}$ with $\alpha \sim 0.5 - 2.0$ (Kong et al. 2012; Takata et al. 2017).

5.2. Energy Spectrum of the High-energy Electron Population

It is commonly assumed that the unshocked electron pairs from the pulsar wind are accelerated to a power-law energy distribution in the termination shock. After these electrons are injected into the downstream post-shock flow, radiative energy losses may change the energy spectrum, creating features that depart from the original power-law shape. The energy spectrum can be described by a broken power law with an exponential cutoff. While the break is the result of the transition from being dominated by ICS, in the Klein–Nishima regime, to being dominated by synchrotron losses (Moderski et al. 2005), the cutoff is the result of the maximum acceleration energy provided by the confinement power of the B -field. Moreover, adiabatic energy losses may also play a relevant role in shaping the electron spectrum (Zabalza et al. 2011).

The electron energy range relevant to describe our observations extends from the electrons responsible for producing the lowest energy X-ray photons (~ 3 keV) through synchrotron emission, up to the ones responsible for producing the highest-energy gamma-ray photons (~ 3 TeV) through ICS. At the upper bound, because the ICS occurs in the Klein–Nishima regime, the contribution from electrons with energy higher than the gamma-ray photons' is negligible, which implies that the maximum relevant electron energy is $E_{e,\text{max}} \lesssim 5$ TeV. At the lower bound, the energy of the electrons that contribute to the production of X-ray photons of energy E_{syn} is given by $E_e = \sqrt{E_{\text{syn}} m_e^3 / eB}$. Because typical B values found in gamma-ray binaries are in the range of 0.1–5 G (Dubus 2013), the minimum relevant electron energy is $E_{e,\text{min}} \approx 0.1$ TeV.

The maximum acceleration energy is estimated by balancing the acceleration and the energy-loss timescales, where the latter is dominated by the synchrotron losses at the highest energies (Khanguyan et al. 2008). For typical parameters found in gamma-ray binaries, we determined that $E_{e,\text{max}} > 10$ TeV (Zabalza et al. 2011; Dubus 2013). The break energy, on the other hand, is expected to be $\sim 0.1 - 0.5$ TeV for typical conditions during our observations of HESS J0632+057, which translates into a break in the X-ray synchrotron spectrum. As the SED derived from our X-ray observations does not show any indication of deviation from a single power law, we assume here that the electron energy break appears at $E_e < 0.1$ TeV. Therefore, the electron spectrum will be assumed to follow a single power law of the form $dN_e/dE_e = N_e(E_e/1 \text{ TeV})^\Gamma$ in the energy range 0.1–5 TeV. The adiabatic energy losses do not affect this assumption

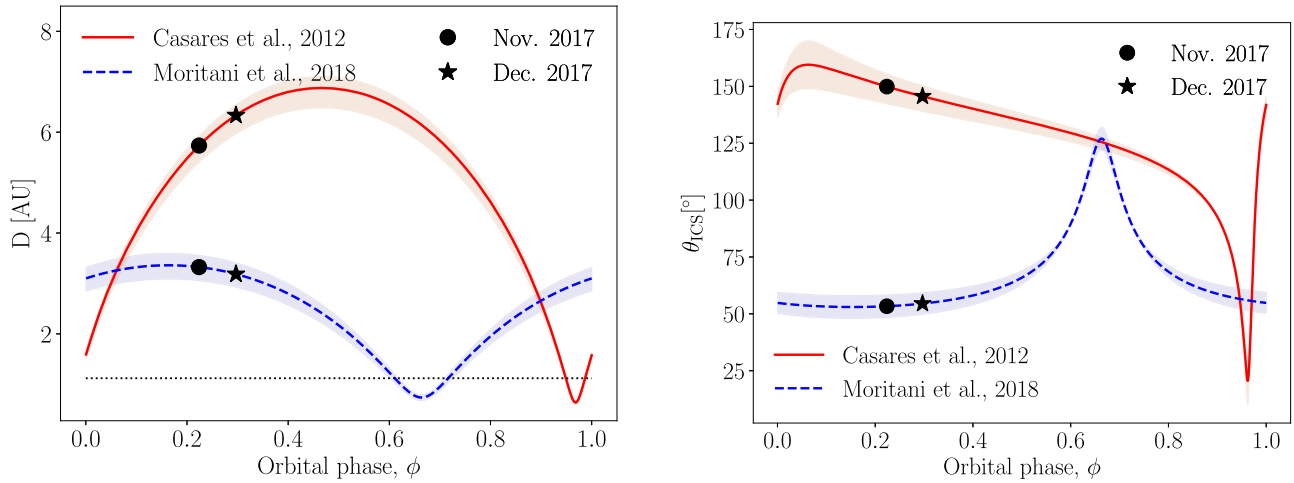


Figure 4. Distance between the Be star and the pulsar (left) and ICS angle (right) derived from the orbital solutions by Casares et al. (2012) and Moritani et al. (2018). The black markers indicate our two sets of observations, the dashed black line in the left panel indicates the estimated size of the circumstellar disk, and the colored bands indicate the uncertainties due to the system’s inclination (see text for details).

because it is only expected to change the normalization and the slope of the spectrum, without creating any features. Thus, our model relies only on minimal assumptions about the electron spectrum, which is only possible due to the large overlap between the energies of the electrons responsible for producing hard X-rays through synchrotron emission and TeV gamma-rays through ICS emission.

5.3. Radiative Processes

The population of high-energy electrons accelerated at the termination shock is assumed to radiate through synchrotron and ICS, producing the X-ray and gamma-ray photons observed at Earth, respectively. The B -field responsible for the synchrotron emission is calculated following Equation (3). The seed photon field for the ICS is composed of the thermal photons radiated by the companion star, with a density given by

$$U = \frac{\sigma_{\text{SB}} T_{\text{Be}}^4 R_{\text{Be}}^2}{c(D - R_{\text{sh}})^2}, \quad (5)$$

where σ_{SB} is the Stefan–Boltzmann constant. We also account for the anisotropic nature of the ICS by calculating the photon scattering angle (θ_{ICS}) from the geometry given by the orbital solutions.

Because of the relatively dense field provided by the stellar photons, the impact of pair-production absorption of gamma-rays (Gould & Schröder 1967) becomes relevant. For each evaluation of the model, we calculate the optical depth ($\tau_{\gamma\gamma}$) as a function of the gamma-ray photon energy, accounting for the corresponding position of the termination shock and geometry of the system (see e.g., Dubus 2006; Sierpowska-Bartosik & Torres 2008; Sushch & van Soelen 2017 for the details of the $\tau_{\gamma\gamma}$ calculation). The gamma-ray spectrum expected to be observed is then attenuated by a factor of $e^{-\tau_{\gamma\gamma}}$. The impact of pair-production absorption is the strongest at the low end of the observed gamma-ray spectrum (~ 0.2 TeV), and it is larger for the Casares et al. (2012) orbital solution because of the longer path of the gamma-ray photons within the stellar photon field.

5.4. Model Fitting

The model described above was fitted to the SED derived from both *NuSTAR* and VERITAS observations. In what follows, the two observation sets will be labeled by the lower indices 0 and 1, for the 2017 November and December observations, respectively. From the orbital solutions described in Section 4, we calculated the distance between the objects (D) and the ICS angle (θ_{ICS}), which are shown in Figure 4 as a function of the system’s phase. Assumptions are made regarding the stellar wind properties \dot{M}_w and v_w . The impact of the uncertainties on \dot{M}_w will be estimated by repeating the procedure with different values.

The remaining parameters of the model are the pulsar spin-down luminosity (L_{sd}), the pulsar-wind magnetization at termination shock for both periods (σ_0 and σ_1), and the parameters of the electron spectrum for both periods ($N_{e,0}$, Γ_0 , $N_{e,1}$ and Γ_1). The dependence of σ on R_{sh} is assumed to constrain σ_0 and σ_1 and reduce them to a single parameter. Here, we maintained σ_0 as a free parameter of the model and we calculated $\sigma_1 = \sigma_0 \left(\frac{R_{\text{sh},0}}{R_{\text{sh},1}}\right)^\alpha$, with $\alpha = 1$. As the difference between $R_{\text{sh},0}$ and $R_{\text{sh},1}$ is relatively small for our observations, the impact of the choice of $\alpha = 1$ is minimal.

Regarding the electron spectrum, only $N_{e,0}$ and $N_{e,1}$ were treated as free parameters, while Γ_0 and Γ_1 were set to the values derived from the single power-law fit of the X-ray spectrum (see Section 3). The values are $\Gamma_0 = 1.77 \times 2 - 1 = 2.54$ and $\Gamma_1 = 1.56 \times 2 - 1 = 2.12$. In the end, the model contains four free parameters: L_{sd} , σ_0 , $N_{e,0}$ and $N_{e,1}$.

The model evaluation starts by inserting L_{sd} into Equations (1) and (2) to calculate $R_{\text{sh},0}$ and $R_{\text{sh},1}$ (using the assumptions of \dot{M}_w and v_w and D_0/D_1 given by the orbital solutions). With R_{sh} , the photon density U of the ICS seed field and the optical depth $\tau_{\gamma\gamma}$ are calculated. In the following, the values of the B -field at the shock, B_0 and B_1 , are calculated by inserting the σ and R_{sh} values in Equation (3). Finally, with the electron spectrum determined by $N_{e,0}$ and $N_{e,1}$, the synchrotron and ICS spectra are calculated, using θ_{ICS} from the orbital solutions for the ICS emission.

The synchrotron and ICS emission were computed by following Blumenthal & Gould (1970) using the Naima package (Zabalza 2015). The SED fit is performed by means

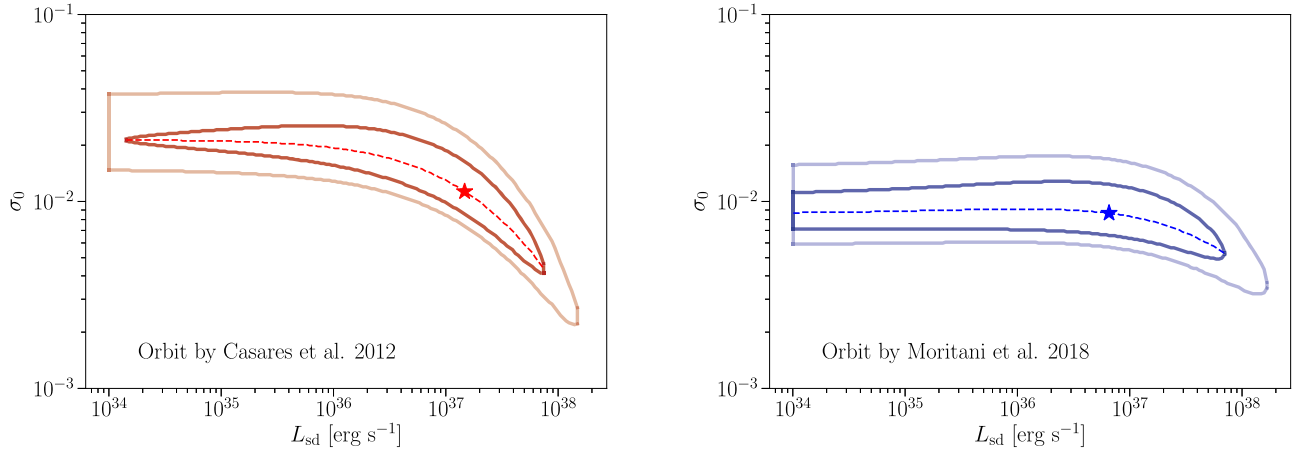


Figure 5. Results of the model fitting in the $L_{\text{sd}}-\sigma_0$ plane for the sets of orbital parameters from Casares et al. (2012) (left) and Moritani et al. (2018) (right). The best solution is indicated by a star while the 1 and 2σ regions are indicated by the darker and lighter continuous lines, respectively. The dashed lines show the values of σ_0 that minimize the χ^2 for each value of L_{sd} .

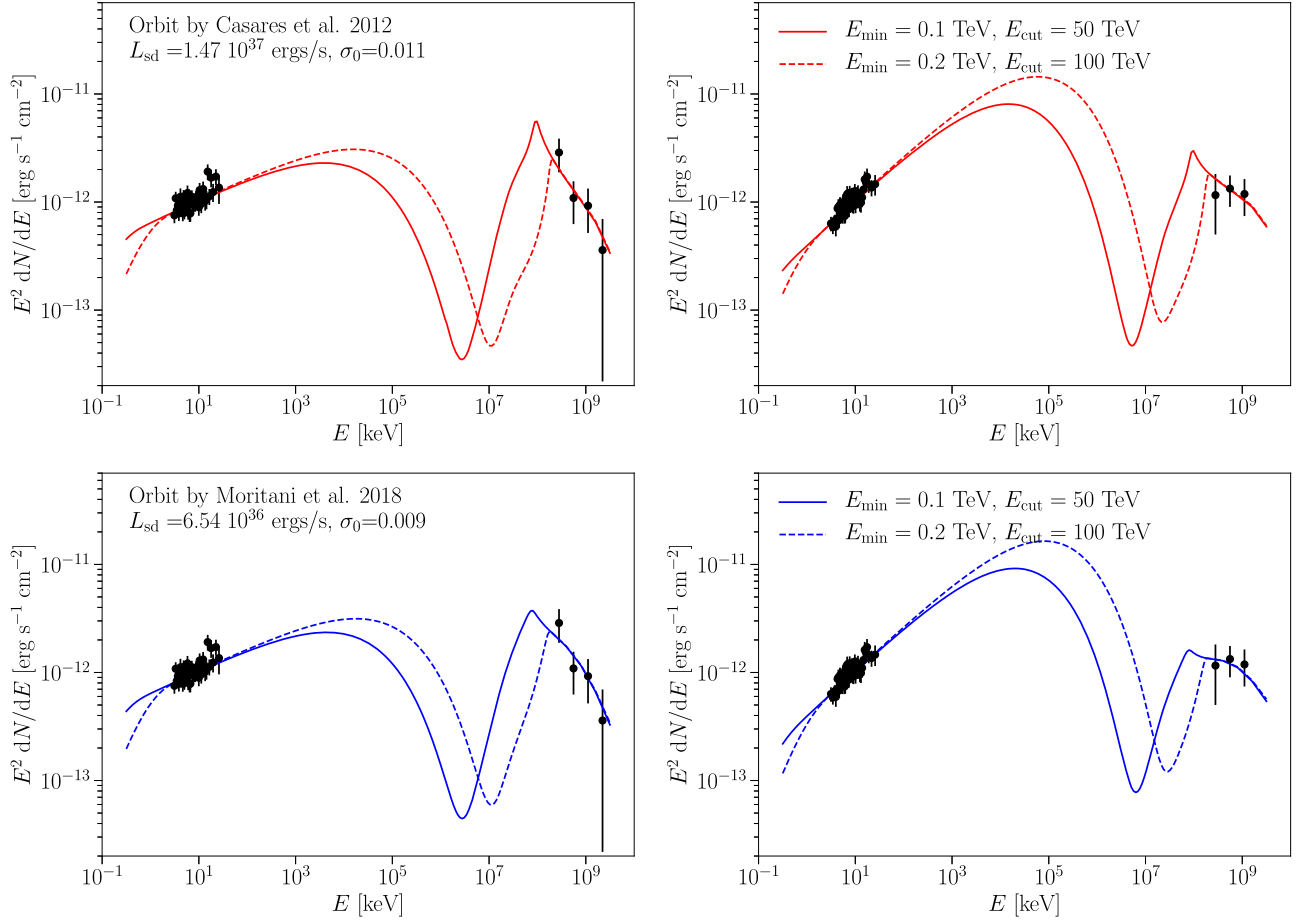


Figure 6. SED data–model comparison assuming the best solution of the model fitting for the Casares et al. (2012) (upper) and Moritani et al. (2018) (lower) orbital solutions. The 2017 November and December observations are shown in the left and right panels, respectively. The different line styles indicate different assumptions of E_{min} and E_{cut} .

of a χ^2 method. While L_{sd} and σ_0 are scanned over a predefined grid, $N_{e,0}$ and $N_{e,1}$ are fitted by minimizing χ^2 using Minuit framework (James & Roos 1975).

6. Results

We show in Figure 5 the results of the fit for the $L_{\text{sd}}-\sigma_0$ plane, indicating the 1 and 2σ regions for both orbital solutions.

The best solutions are indicated by stars and the corresponding χ^2/dof is 0.786 for both sets of orbital parameters. The dashed lines indicate the σ_0 that minimizes the χ^2 for each value of L_{sd} . These curves will be labeled as *best curves* in what follows. The SED model–data comparisons are shown in Figure 6, in which the best solution of the fit is used to evaluate the model. To illustrate the SED throughout all the energy bands, the electron spectrum was assumed to be a power law, starting at

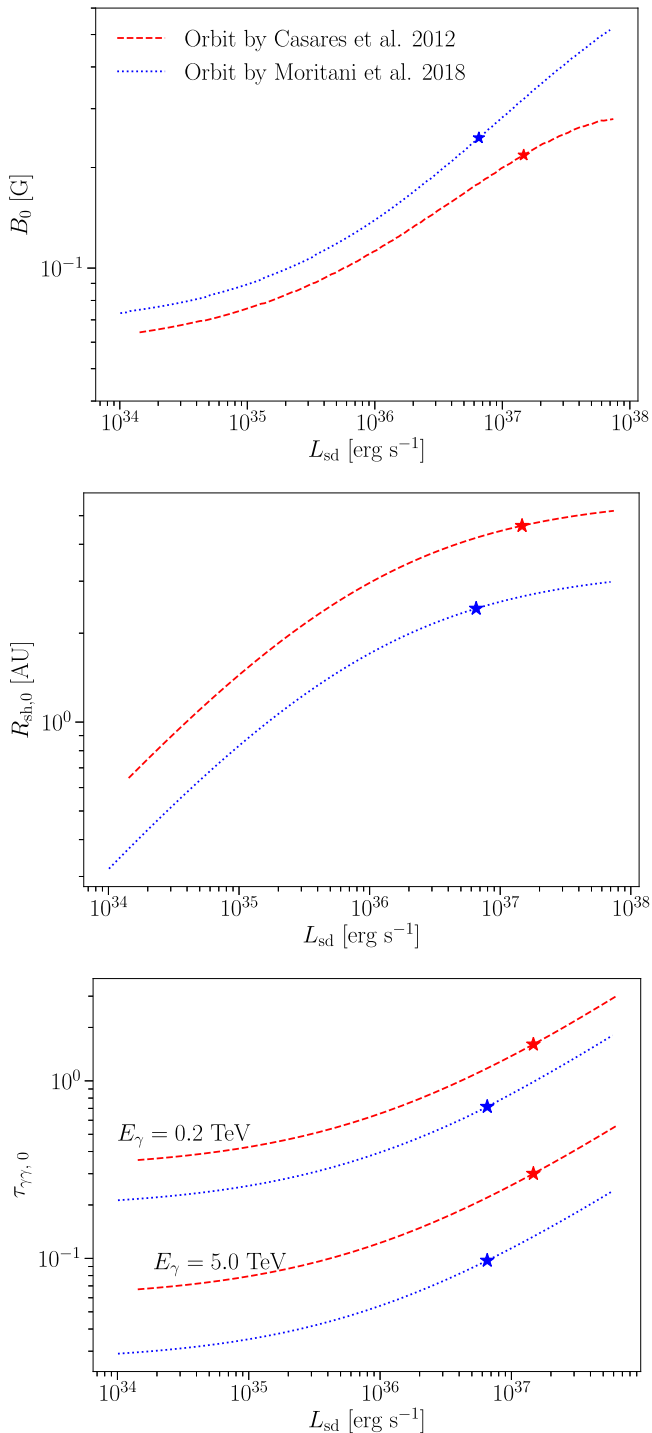


Figure 7. B -field (upper), shock distance to the pulsar (middle) and pair-production optical depth (lower) for the earlier set of observations as a function of L_{sd} . The lines represent the best curves and the stars show the best solutions. The optical depth $\tau_{\gamma,0}$ is shown for gamma-ray photon energies of 0.2 (upper lines) and 5.0 TeV (bottom lines).

E_{min} , with an exponential cutoff characterized by E_{cut} . Although different values of E_{min} and E_{cut} are illustrated in Figure 6, the model fitting does not depend on these parameters, as explained in Section 5.2.

The degeneracy observed between L_{sd} and σ_0 implies that neither of these parameters can be individually constrained with our approach. Nevertheless, our results demonstrate that the observations can be consistently described by a pulsar wind

model and indicate the region of the $L_{\text{sd}}\text{-}\sigma_0$ space that allows for it. To further characterize the allowed solutions, we show in Figure 7 the B -field, R_{sh} and $\tau_{\gamma\gamma}$ for the November observation (B_0 , $R_{\text{sh},0}$ and $\tau_{\gamma\gamma,0}$) as a function of L_{sd} . The lines in Figure 7 correspond to the best curves shown in Figure 5.

The estimated total luminosity of the full SED shown in Figure 6 is in the range $10^{34}\text{--}10^{35}$ erg s $^{-1}$. Estimations of the efficiency of nonthermal radiation in gamma-ray binaries are highly uncertain. For instance, *Fermi*-LAT observations show that nearly all the L_{sd} is converted into nonthermal radiation in PSR B1259-63 around the periastron passage (Abdo et al. 2011). Sierpowska-Bartosik & Torres (2008), on the other hand, assume an efficiency of 0.01 for LS 5039. Therefore, the truncation of our results at $L_{\text{sd}} = 10^{34}$ erg s $^{-1}$ represents a conservative lower limit.

The impact of the different system geometries provided by the two orbital solutions is minimal. The observations are equally well described by both sets of orbital parameters, with no indication of one of them being favored. While σ_0 for $L_{\text{sd}} < 10^{37}$ erg s $^{-1}$ is two to three times larger for the Casares et al. (2012) solution, the difference in B_0 amounts to only a factor of 0.6 at the highest L_{sd} regime.

At the high L_{sd} regime of the solutions, the upper limit within 1σ is $L_{\text{sd}} < 7 \times 10^{37}$ erg s $^{-1}$ for both sets of orbital parameters, which is consistent with expectations for very young pulsars. In this regime, the relatively strong pulsar wind moves the termination shock closer to the companion star (see Figure 7, middle). For both orbital solutions, the termination shock is approximately halfway between the stars for the highest L_{sd} values, although the absolute distances are different. The proximity of the shocked region to the Be star implies a larger density for the ICS seed-photon field, and consequently, enhanced ICS emission, but also stronger pair-production absorption. As the ratio between ICS and synchrotron emission is constrained by the data, the B -field has to change accordingly to compensate for the ICS behavior, which is done by changing σ_0 . In this regime, $B_0 \approx 0.25$ and ≈ 0.5 G for the Casares et al. (2012) and Moritani et al. (2018) solutions, respectively.

As the L_{sd} of the solutions decreases, the termination shock moves closer to the pulsar, within a small fraction of the distance between the objects. At this regime, the B -field also decreases and reaches $B_0 \approx 0.06$ and 0.07 G for the Casares et al. (2012) and Moritani et al. (2018) solutions, respectively.

The impact of the uncertainties on the system’s parameters was evaluated by varying the assumed values and repeating the fitting procedure. We found that the most relevant uncertainty is that of the mass-loss rate of the stellar wind, \dot{M}_w . The results of the fit for $\dot{M}_w = 10^{-9.0}$, $10^{-8.5}$ and $10^{-8.0}$ M_\odot yr $^{-1}$ are shown in Figure 8. We also show the results in Figure 9 by accounting for the uncertainties in the system’s inclination. Note that as described in Section 4, the variations of the inclination also result in variations in the semimajor axis, as well as in the mass of the companion star. Apart from the \dot{M}_w and inclination, we also tested the robustness of the results considering the uncertainties in the eccentricity, ω , P_{orb} , and α . In all cases the effect is similar to or slightly larger than that observed for the inclination. The uncertainty range considered for each of these parameters is indicated in Table 1.

The impact of the poorly known properties of the stellar wind, represented by the mass-loss rate \dot{M}_w , is the most relevant source of uncertainty on the constraining power of the pulsar-

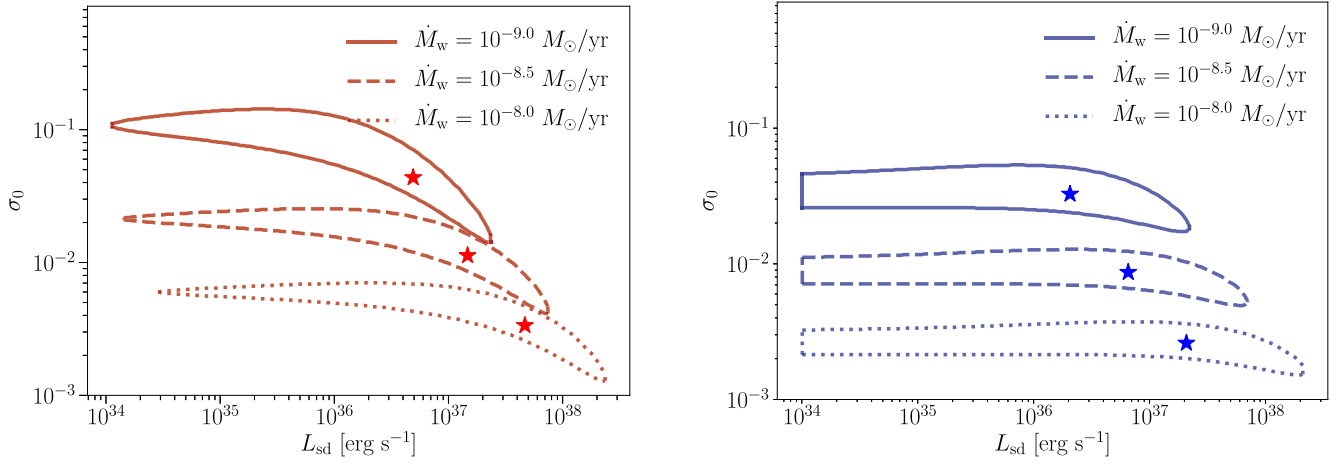


Figure 8. Results of the model fitting in the $L_{\text{sd}}-\sigma_0$ plane for different values of \dot{M}_w within the range $10^{-9}-10^{-8} M_{\odot}\text{yr}^{-1}$. The orbital solutions by Casares et al. (2012) and Moritani et al. (2018) are shown in the left and right panel, respectively. The lines indicate the 1σ region of the parameters.

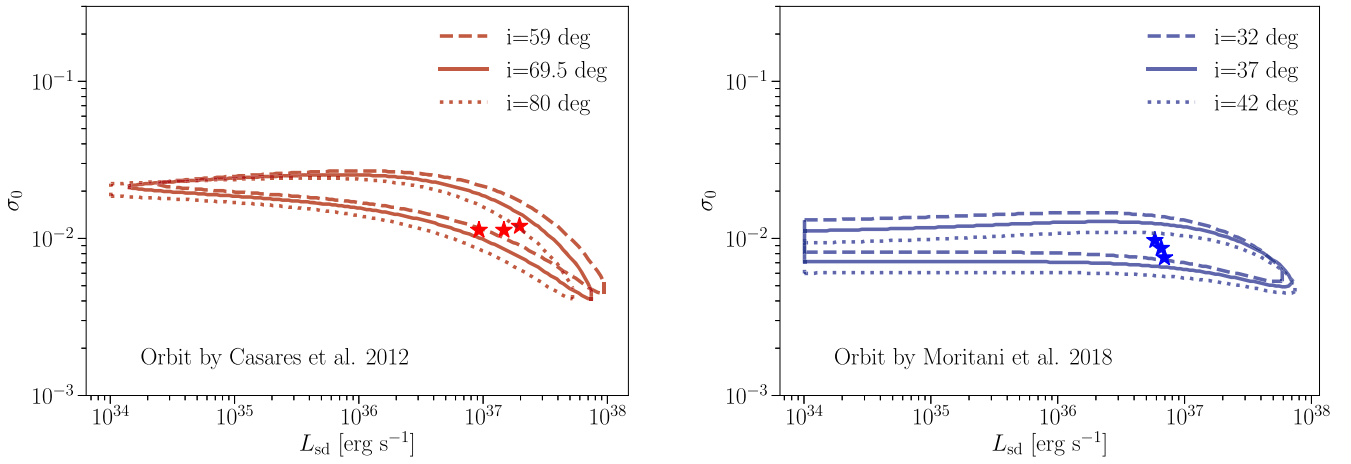


Figure 9. Results of the model fitting in the $L_{\text{sd}}-\sigma_0$ plane for different values of inclination as described in Section 4. The orbital solutions by Casares et al. (2012) and Moritani et al. (2018) are shown in the left and right panel, respectively. The lines indicate the 1σ region of the parameters.

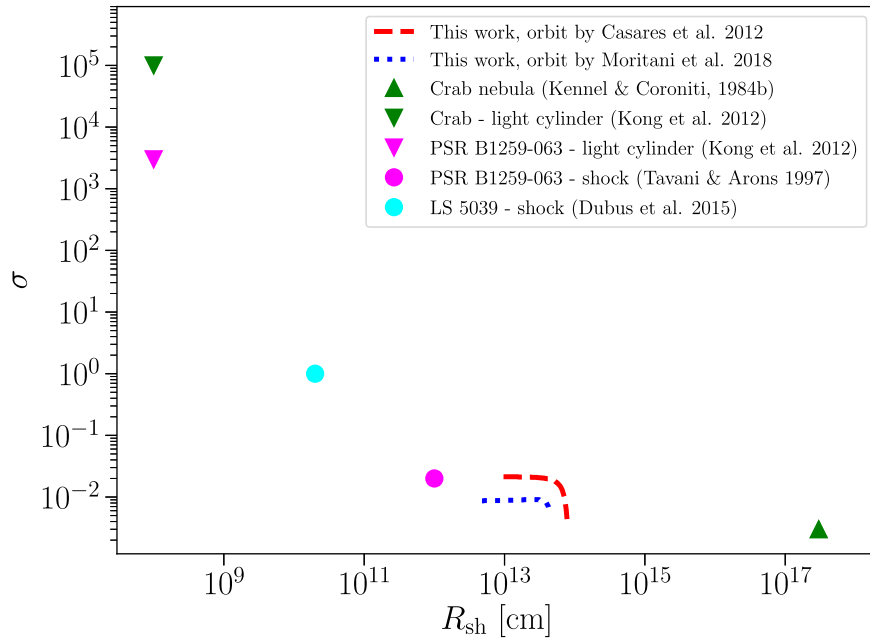


Figure 10. Pulsar-wind magnetization vs R_{sh} , obtained from the results of our model fitting, compared with a selection of theoretical and observational constraints (see text for details).

wind magnetization from our approach. The large range of \dot{M}_w assumed here is sufficient to incorporate any effect due to the presence of the circumstellar disk, which has been neglected by the model assumptions.

7. Summary and Discussions

We presented the results of two sets of combined observations of the gamma-ray binary HESS J0632+057, by *NuSTAR* in the hard X-ray band, and by VERITAS, in the TeV gamma-ray band. These observations correspond to the rise of the first peak observed in the X-ray and TeV light curves, at $\phi \approx 0.22$ and 0.30. The data provided by both instruments allows us to derive the combined SED for these two periods. The spectral and timing analysis performed on the *NuSTAR* observations show that: (a) the spectra are well described by a single power-law model with a spectral hardening observed between the two observations (Γ going from 1.77 ± 0.05 to 1.56 ± 0.05), and (b) no evidence of time variability, red noise, or pulsation has been found, consistent with observations of other gamma-ray binaries.

The SED data is used to probe a model based on the pulsar-wind scenario, in which the nonthermal emission is produced by high-energy electrons accelerated at the termination shock formed by the interaction between pulsar and stellar wind. The applied model relies on a minimum number of assumptions which are sufficient for the description of the observations presented in this paper. The description of further observations would require to expand the number of assumptions and the complexity of the model.

The model fitting benefited from two characteristics of our observations. First, for both orbital solutions, the observations correspond to periods in which the distance between the Be star and the compact object is sufficiently large so that the influence of the circumstellar disk is negligible, reducing the number of assumptions required to describe the properties of the stellar wind. second, in systems like gamma-ray binaries, there is a large overlap between the energy range of the electrons responsible for producing hard X-rays and very-high-energy gamma-rays (through synchrotron and ICS, respectively), which allows us to simplify the assumptions about the shape of the electron spectrum to a single power-law description, with only two parameters.

The results of the model fitting show the regions of the $L_{sd}-\sigma$ plane that are allowed by our data. We find an upper limit of $L_{sd} < 7 \times 10^{37} \text{ erg s}^{-1}$ within 1σ , independent of the orbital solution, which is consistent with expectations of young pulsars. The σ parameter is constrained to be 0.003–0.03 at the location of the shock. Constraints on σ are particularly important for understanding the physical process behind the transport of energy from the rotation powered pulsar to the surrounding medium, which is still a subject of intense discussions (Arons 2002; Kirk et al. 2009). While theoretical models predict that at the light cylinder the pulsar wind is dominated by Poynting energy ($\sigma_L \gg 1$), observations of the Crab Nebula constrain σ at much larger distances to be kinetic particle dominated ($\sigma_N \ll 1$). The transition between these two regimes is not well described within the current theoretical framework, originating the so-called “ σ problem.” In gamma-ray binaries, the pulsar-wind termination is typically located at intermediate distances between the light cylinder and the termination shock in pulsar-wind nebulae, which makes these systems interesting in this context.

In Figure 10 we compare the σ versus R_{sh} of the best curves obtained from our fitting with the following selection of results: (a) at the light cylinder ($R_{sh} \approx 10^8 \text{ cm}$), Kong et al. (2012) estimates theoretically that $\sigma \approx 1 \times 10^5$ and 8×10^3 for the Crab Pulsar and for PSR J1259–63, respectively, (b) Tavani & Arons (1997) assume $\sigma = 0.02$ at the termination shock to describe observations of PSR J1259–63 around the periastron, (c) Dubus et al. (2015) constrains $\sigma \approx 1$ at the termination shock to describe observations of the system LS 5039 using a numerical hydrodynamical model and (d) the classical result by Kennel & Coroniti (1984b) that constrains $\sigma \approx 0.003$ at $R_{sh} \approx 10^{17} \text{ cm}$ for the Crab Nebula. The comparison indicates that all systems follow a similar trend of σ decreasing with R_{sh} . The consistency observed between our results and other systems provides further support to the pulsar scenario of HESS J0632+057.

This work used data from the *NuSTAR* mission, a project led by the California Institute of Technology, managed by the Jet Propulsion Laboratory, and funded by NASA. We made use of the *NuSTAR* Data Analysis Software (NuSTARDAS) jointly developed by the ASI Science Data Center (ASDC, Italy) and the California Institute of Technology (USA).

This research is supported by grants from the U.S. Department of Energy Office of Science, the U.S. National Science Foundation and the Smithsonian Institution, and by NSERC in Canada. We acknowledge the excellent work of the technical support staff at the Fred Lawrence Whipple Observatory and at the collaborating institutions in the construction and operation of the VERITAS instrument.

Facilities: *NuSTAR*, VERITAS.

Software: HEASoft (v6.22), Stingray (Huppenkothen et al. 2016), NuSTARDAS (v1.8.0), XSPEC (v12.9.1; Arnaud 1996), Naima (Zabalza 2015).

ORCID iDs

W. Benbow  <https://orcid.org/0000-0003-2098-170X>
 R. Bird  <https://orcid.org/0000-0002-4596-8563>
 Q. Feng  <https://orcid.org/0000-0001-6674-4238>
 L. Fortson  <https://orcid.org/0000-0002-1067-8558>
 A. Furniss  <https://orcid.org/0000-0003-1614-1273>
 G. H. Gillanders  <https://orcid.org/0000-0001-8763-6252>
 D. Hanna  <https://orcid.org/0000-0002-8513-5603>
 P. Kaaret  <https://orcid.org/0000-0002-3638-0637>
 D. Kieda  <https://orcid.org/0000-0003-4785-0101>
 M. Krause  <https://orcid.org/0000-0001-7595-0914>
 G. Maier  <https://orcid.org/0000-0001-9868-4700>
 D. Nieto  <https://orcid.org/0000-0003-3343-0755>
 N. Park  <https://orcid.org/0000-0002-4282-736X>
 M. Pohl  <https://orcid.org/0000-0001-7861-1707>
 R. R. Prado  <https://orcid.org/0000-0001-9152-2995>
 E. Pueschel  <https://orcid.org/0000-0002-0529-1973>
 M. Santander  <https://orcid.org/0000-0001-7297-8217>
 I. Sushch  <https://orcid.org/0000-0002-2814-1257>
 P. Wilcox  <https://orcid.org/0000-0003-3268-7006>

References

- Abdo, A. A., Ackermann, M., Ajello, M., et al. 2011, *ApJL*, 736, L11
 Acciari, V. A., Aliu, E., Arlen, T., et al. 2009, *ApJL*, 698, L94
 Acciari, V. A., Bellicke, M., Blaylock, G., et al. 2008, *ApJ*, 679, 1427
 Aharonian, F. A., Akhperjanian, A. G., Bazer-Bachi, A. R., et al. 2007, *A&A*, 469, L1

- Aleksić, J., Alvarez, E. A., Antonelli, L. A., et al. 2012, *ApJL*, 754, L10
- Aliu, E., Archambault, S., Aune, T., et al. 2014, *ApJ*, 780, 168
- Aragona, C., McSwain, M. V., & De Becker, M. 2010, *ApJ*, 724, 306
- Arnaud, K. A. 1996, in ASP Conf. Ser. 101, *Astronomical Data Analysis Software and Systems V*, ed. G. H. Jacoby & J. Barnes (San Francisco, CA: ASP), 17
- Arons, J. 2002, in ASP Conf. Ser. 271, *Neutron Stars in Supernova Remnants*, ed. P. O. Slane & B. M. Gaensler (San Francisco, CA: ASP), 1533
- Bachetti, M., Harrison, F. A., Cook, R., et al. 2015, *ApJ*, 800, 109
- Ball, L., & Kirk, J. G. 2000, *Aph*, 12, 335
- Blumenthal, G. R., & Gould, R. J. 1970, *RvMP*, 42, 237
- Bongiorno, S. D., Falcone, A. D., Stroh, M., et al. 2011, *ApJL*, 737, L11
- Casares, J., Ribó, M., Ribas, I., et al. 2012, *MNRAS*, 421, 1103
- Corbet, R. H. D., Chomiuk, L., Coe, M., et al. 2019, *ApJ*, 884, 93
- Daniel, M. K. & VERITAS Collaboration 2007, ICRC (Merida), 30, 1325
- Dubus, G. 2006, *A&A*, 451, 9
- Dubus, G. 2013, *A&ARv*, 21, 64
- Dubus, G., Lamberts, A., & Fromang, S. 2015, *A&A*, 581, A27
- Falcone, A. D., Grube, J., Hinton, J., et al. 2010, *ApJL*, 708, L52
- Fomin, V. P., Stepanian, A. A., Lamb, R. C., et al. 1994, *Aph*, 2, 137
- Gould, R. J., & Schröder, G. P. 1967, *PhRv*, 155, 1404
- Harding, A. K., & Gaisser, T. K. 1990, *ApJ*, 358, 561
- Harrison, F. A., Craig, W. W., Christensen, F. E., et al. 2013, *ApJ*, 770, 103
- Hillas, A. M. 1985, ICRC (San Diego), 19, 445
- Hinton, J. A., Skilton, J. L., Funk, S., et al. 2009, *ApJL*, 690, L101
- Ho, W. C. G., Ng, C.-Y., Lyne, A. G., et al. 2017, *MNRAS*, 464, 1211
- Holder, J., Atkins, R. W., Badran, H. M., et al. 2006, *Aph*, 25, 391
- Huppenkothen, D., Bachetti, M., Stevens, A. L., et al. 2016, *Stingray: Spectral-timing software*, Astrophysics Source Code Library, ascl:1608.001
- James, F., & Roos, M. 1975, *CoPhC*, 10, 343
- Kennel, C. F., & Coroniti, F. V. 1984a, *ApJ*, 283, 694
- Kennel, C. F., & Coroniti, F. V. 1984b, *ApJ*, 283, 710
- Khangulyan, D., Aharonian, F., & Bosch-Ramon, V. 2008, *MNRAS*, 383, 467
- Kirk, J. G., Lyubarsky, Y., & Petri, J. 2009, in *Neutron Stars and Pulsars*, ed. W. Becker (Berlin: Springer), 421
- Kong, S. W., Cheng, K. S., & Huang, Y. F. 2012, *ApJ*, 753, 127
- Krawczynski, H., Carter-Lewis, D. A., Duke, C., et al. 2006, *Aph*, 25, 380
- Li, J., Torres, D. F., Cheng, K.-S., et al. 2017, *ApJ*, 846, 169
- Madsen, K. K., Harrison, F. A., Markwardt, C. B., et al. 2015, *ApJS*, 220, 8
- Maier, G., & Holder, J. 2017, ICRC (Busan), 35, 747
- Mirabel, I. F., & Rodríguez, L. F. 1998, *Natur*, 392, 673
- Moderski, R., Sikora, M., Coppi, P. S., et al. 2005, *MNRAS*, 363, 954
- Mori, K., Gotthelf, E. V., Hailey, C. J., et al. 2017, *ApJ*, 848, 80
- Moritani, Y., Kawano, T., Chimasu, S., et al. 2018, *PASJ*, 70, 61
- Moritani, Y., Okazaki, A. T., Carciofi, A. C., et al. 2015, *ApJL*, 804, L32
- Paredes, J. M., & Bordas, P. 2019, arXiv:1902.09898
- Park, N. & VERITAS Collaboration 2015, ICRC (The Hague), 34, 771
- Sierpowska-Bartosik, A., & Torres, D. F. 2008, *Aph*, 30, 239
- Snow, T. P. 1981, *ApJ*, 251, 139
- Sushch, I., & van Soelen, B. 2017, *ApJ*, 837, 175
- Takata, J., Tam, P. H. T., Ng, C. W., et al. 2017, *ApJ*, 836, 241
- Tavani, M., & Arons, J. 1997, *ApJ*, 477, 439
- Waters, L. B. F. M., van den Heuvel, E. P. J., Taylor, A. R., et al. 1988, *A&A*, 198, 200
- Weekes, T. C., Badran, H., Biller, S. D., et al. 2002, *Aph*, 17, 221
- Zabalza, V. 2015, ICRC (The Hague), 34, 922
- Zabalza, V., Paredes, J. M., & Bosch-Ramon, V. 2011, *A&A*, 527, A9
- Zamanov, R., Martí, J., & García-Hernández, M. T. 2017, *BlaAJ*, 27, 57
- Zamanov, R. K., Stoyanov, K. A., Martí, J., et al. 2016, *A&A*, 593, A97